Image analysis for the time-resolved description of microparticle resuspension under transient airflow

Corentin Cazes, Lionel Fiabane, Félicie Theron, Dominique Heitz, Laurence Le Coq

Image analysis for the time-resolved description of microparticle resuspension under transient airflow

Corentin Cazes[a,b], Lionel Fiabane[a,*], Félicie Theron[b], Dominique Heitz[a], Laurence Le Coq[b]

[a] *INRAE, OPAALE, 17, Avenue de Cucillé, CS 64427, Rennes, 35000, France*
[b] *IMT Atlantique, CNRS, GEPEA, 4, Rue Alfred Kastler, CS 20722, Nantes, 44307, France*

Abstract

This paper presents an automatic particle detection algorithm to study the time-resolved resuspension of isolated microparticle mono-layers exposed to airflow acceleration followed by steady-state. The algorithm post-processes movies of the deposit behaviour and returns the particle number, the granulometry, and the homogeneity of each frame. It allows the detection and isolation of the particle clusters to process them separately. The algorithm is validated using both synthetic images, and experimental datasets corresponding to ventilated duct cases. The number of particles remaining on the surface over time is returned, and correlations can be made with instantaneous physical parameters of the flow (e.g., centre or friction velocity). The algorithms and data are available online: see Cazes et al. (2023); CAZES et al. (2023), respectively.

Keywords: Microparticle resuspension, Automatic image processing, Particle count, Time-resolved resuspension

1. Introduction

The particle resuspension phenomenon that involves the detachment and re-entrainment of a particle from a surface due to an airflow plays an essential role in various industrial applications such as semiconductor manufacturing, pharmaceutical production, nuclear maintenance, or dust entrainment linked to human activities (Gradoń, 2009; Evangeliou et al., 2016; Qian et al., 2014). In particular, understanding this phenomenon enables the prediction of airborne particulate contamination, especially in Heating, Ventilation, and Air-Conditioning (HVAC) systems (D'Alicandro et al., 2021; Kottapalli and Novosselov, 2021; Raveh-Amit et al., 2022). The scope of this study is the resuspension of mono-layer spherical-shaped microparticles during fan acceleration in a ventilated duct. The flow is accelerated from zero velocity to a short steady state period to reproduce situations encountered during the start of HVAC systems in a building after shutdown (night or weekend) or maintenance.

An isolated particle deposited on a surface and exposed to airflow experiences two forces that compete: the adhesion and the aerodynamic forces. Eventually, the aerodynamic forces overcome the adhesion forces, and the particle detaches from the surface. Straight after detachment, the particle may either have a motion on the surface before being drawn into the flow (rolling or sliding motion) or a direct lift-off (Kassab et al., 2013). High concentration can cause collisions between particles (Rondeau et al., 2021), leading to either resuspension of these particles or stopping the moving particle. Previous studies involved mono-layer deposits of isolated particles to limit particle interactions (Ibrahim and Dunn, 2006). It also limits the particle cluster number and makes the particle count easier. Many models assume the particles to have a spherical shape (e.g. Benito et al., 2015) for symmetry and contact description between the particles and the surface. Other parameters can also influence the resuspension phenomenon, such as humidity, temperature, or electrostatic forces between particles and surface (Henry and Minier, 2014a; Nasr et al., 2019).

Some authors count particles before and after each experiment to track the particle number. For instance, Barth et al. (2014) use an optical microscope system coupled with an image analysis procedure, and Krauter and Biermann

*Corresponding author.
Email address: lionel.fiabane@inrae.fr (Lionel Fiabane)

(2007) collect the samples after each experiment using swabs and then analyse them. These experiments give the fraction of detached particles over a significant time, whatever the temporal airflow pattern used. However, this does not capture the particle behaviour, and the dynamics of resuspension coupled with transient airflow effects still need to be included. Other studies aim at recording an image of the deposit at each velocity increment (Goldasteh et al., 2013; Vincent et al., 2019), which results in a low acquisition frequency of 1 Hz. Thus, the protocol does not depict the temporal behaviour of the deposit during the short transition period.

To analyse the phenomenon through time, it appears more accurate to adopt an Eulerian approach, consisting of the temporal description of number of particles on a fixed area by optical observation. It gives the particle number over time, which leads to the temporal evolution of the remaining particle fraction on the surface defined as:

$$F_{\mathrm{rem}}(t) = \frac{N_{\mathrm{p}}(t)}{N_{\mathrm{p}}(t=0)} \times 100, \tag{1}$$

where N_{p} is the particle number at time t. One can also define the detachment fraction as $F_{\mathrm{det}} = 100 - F_{\mathrm{rem}}$. The previous experimental investigations that used Eulerian tracking (Ibrahim et al., 2003, 2004) were conducted with linear accelerations and provided results regarding resuspended fraction as a function of mean velocity characteristics. Thus, the results do not reflect the temporal dynamic of the phenomenon. Other authors, such as Kassab et al. (2013), studied the resuspension process during fan accelerations with a high acquisition frequency of 2 kHz but did not provide any results concerning the temporal evolution of the airflow properties. As a result, one cannot make correlations between resuspension and flow dynamics.

Previous works from Theron et al. (2020, 2022) highlight that most particles resuspend during the acceleration regime, which happens in a relatively short time. Thus, one has to tackle the problem dynamically to link the resuspension process to the transient flow events. It emphasises the need to track the particle number in a time-resolved way along with the flow characteristics. The acceleration values for HVAC systems are up to $2\,\mathrm{m\,s^{-2}}$ to reach velocity up to several meters per second from zero speed fan. Thus, the transient period is in the range of 2 to 4 seconds, which underlines the need for a significant acquisition frequency value to capture the dynamic of the resuspension phenomenon leading to a high number of images to analyse.

Besides the acquisition frequency, other parameters are essential to ensure accurate optical measurements. As the study focuses on mono-layer of isolated microparticles, the image resolution and the size of the observed window are critical to capture a representative sample of individual particles accurately. These parameters are linked with the acquisition frequency together with the exposure time of the optical system (Agüí and Jiménez, 1987). To have a statistically representative value of F_{rem} (computed with equation 1), one needs a large number of particles. In addition, for a given particle size range, the window size is limited to ensure a high resolution to measure particles' geometrical properties. As a result, one has to compromise between acquisition number and concentration (defined as particle number per area unit), and a large number of experiments must be conducted. This procedure leads to a tremendous number of images to process. Consequently, it requires a post-treatment solution that must be automatic and fast. Moreover, it requires reliability to have high confidence in the detected particle number and to perform advanced analysis such as particle size distribution or other deposit characteristics.

The conventional detection algorithms involve the basic algorithm steps, which consist of image filtration, thresholding, particle boundary definition and particle position refinement (Suji and Bhadauria, 2021). A multitude of algorithms exists for many fields that need detection tools. Nevertheless, they all use the same step procedure as the algorithm developed in the present paper. As Giering et al. (2020) pointed out, the challenge with these algorithms is knowing whether a pixel is part of an object or of the background. In that sense, they focus on the differences between thresholding techniques and edge detection. Sezgin and Sankur (2004) classify the methods into seven groups. One of the best-known techniques is the clustering-based method used when a peak in the grey-scale level histogram is small or hidden by noise (Vrabel et al., 2017). When detecting spherical particles, focusing on the roundness of an object in the image is essential. Canny (1986) developed the well-known Canny edge detector involving computations of mathematical properties of intensity gradients and tangent contour directions to detect the contour of a particle. Since then, it has been enhanced in terms of robustness for noise reduction and complex images. For instance, Meng et al. (2018) use a local adaptive Canny edge detection that divides a frame into sub-images and subsequently computes high and low thresholds to detect particles with different shades. Limits of such algorithms have been addressed by Marsh et al. (2018): they highlight that threshold and watershed techniques coupled with user input parameters deform

the shape of the particle and its centre position. Marsh et al. (2018) address this shortcoming using the Hessian Blob Algorithm, which provides sub-pixel detection of an object with precise centre position and edging. However, their study focuses on molecule detection for Atomic Force Microscopy scans that do not have flat backgrounds, which require pre-processing for conventional particle detection.

Since one of the problems of image processing is quantifying the number of particles in each image, it must be accompanied by uncertainty calculations to assess the algorithm's reliability. Previous studies on resuspension using particle detection algorithms provided neither information on their routines, the validation, nor the reliability of the particle count. In addition, the treatment of potential agglomerates that may exist is never addressed. Very few authors provide their uncertainties regarding the remaining particle fraction: Braaten (1994) assumes a counting error of 0.28 %, and Jiang et al. (2008) report an experimental error of about 10 %. However, these experiments were conducted with a low initial concentration of around 5 part.mm^{-2}, which does not represent enough particles to perform statistical analysis. Moreover, the representativeness of the data used (particle or experiment number) must be included.

This paper aims to tackle these issues. It focuses on an algorithm for microparticle detection and its applications to mono-layer of isolated particles resuspension study. It is organised as follows: in the first part, we describe the steps of the algorithm to detect particles and to discriminate those belonging to clusters; the data acquisition is explained for both experimental and synthetic cases; next, we present the results after applying the algorithm to our data sets, and some possible applications of this post-treatment to study particle resuspension. Finally, limitations and new possible insights offered by the algorithm and applications for particle resuspension are discussed.

2. Algorithm description

The optical tracking acquisitions provide movies that consist of 2560 frames corresponding to the maximum buffer capacity of the computer. Each frame from acquisitions (see an example in Figure 3a) is post-processed to obtain characteristics of the deposit and the number of particles within the frame. This section describes the process performed for one frame. The routines are then repeated for each frame of the movie. The routines are developed using MATLAB, which offers the Image Processing Toolbox with several reference-standard algorithms. The algorithm as well as the data are accessible (see Cazes et al., 2023; CAZES et al., 2023, respectively). Still, similar routines can be created using other programming languages (e.g., C++ and the OpenCV library, Python and either the OpenCV or the Scikit-Image libraries) or image processing software.

The algorithm input consists of a raw grayscale. This image is then processed to obtain a final binarised image with separated particles. Further features can be obtained from this final image, such as the number of particles, the homogeneity of the deposit or the granulometry. An overview of the algorithm is presented on the flowchart in Figure 1. It follows the typical steps of a colloidal detection algorithm which are (Crocker and Grier, 1996):

1. restoration of the image;
2. identification of the particle locations;
3. refinement of the location and removal of the 'wrong' particles.

To produce the experimental data sets, the particles are deposited using an aerosol generator plugged into a deposition chamber. The particles are introduced into the chamber, and after homogenisation of the aerosol, a valve opens and the particles sediment on the surface by gravitation. The chamber is made of PVC, which may induce electrostatic forces and particle-wall and particle-particle interactions. Due to this process, some particles can be stuck together, forming clusters on the deposition surface. It induces an error source during the particle count as the algorithm detects objects; it tallies the cluster as an object but does not detect the particles that constitute the cluster. Thus, the algorithm must be able to distinguish particles within an agglomerate to return the correct particle number.

The algorithm uses different routines that can be described as follows:

Restoration. The restoration converts the raw frame into an integer matrix which represents the pixel value of the grayscale image level. It enables the application of arithmetic operations on the image during post-processing. One of the first operations of interest is the subtraction of a background image (background subtraction) to remove possible noise and any information coming from the camera focal plane (Gonzalez and Woods, 2007). Some other operations can be implemented at this step, such as noise reduction or contrast enhancement. Nevertheless, we keep the algorithm

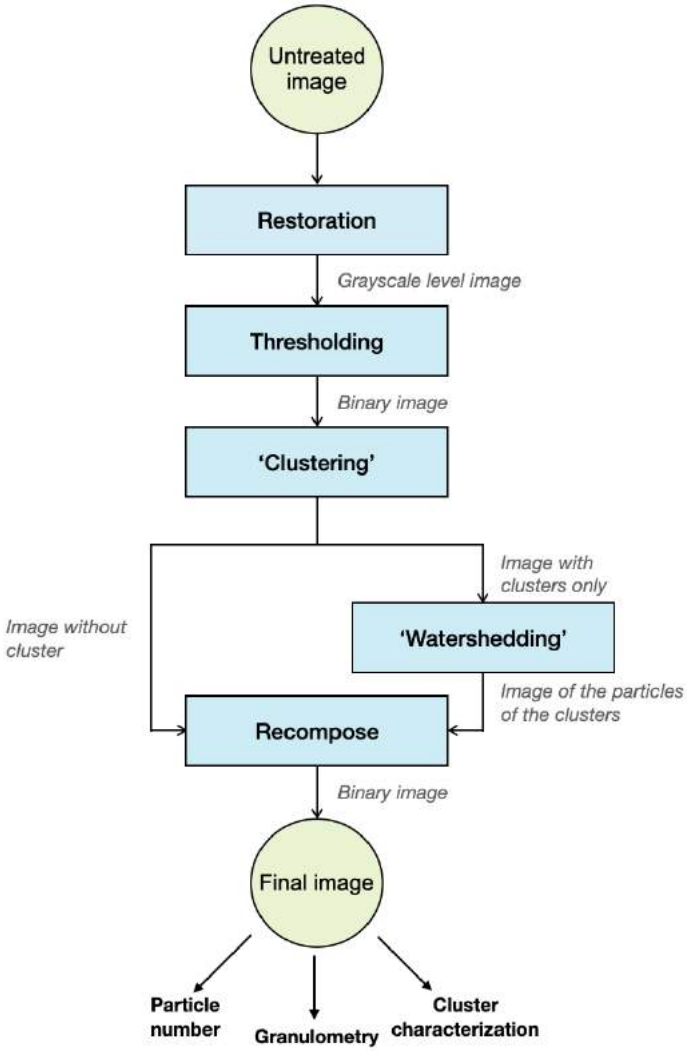

Figure 1: Flowchart of the image processing algorithm.

as simple as possible in this article and only perform a background subtraction. The actual operation is the subtraction of the image we analyse from the background image: it results in an image with bright particles on a dark background that is more convenient to analyse for the operator.

Thresholding. The thresholding is the operation that segregates the pixels of the image between those belonging to the particles from those belonging to the background. Technically, it consists of applying the algorithm developed by Otsu (1979) that computes the threshold value by maximising the inter-class variance σ using the histogram of the grayscale image $\sigma^2 = \omega_1\omega_2\,(\mu_1 - \mu_2)^2$, with ω_i the probability to be in the i-th class and μ_i the mean of the i-th class. Figure 2 shows a typical image histogram for bright particles on a dark background, with the inter-class variance in red. The maximum value of the inter-class variance (black dotted line) is the sought threshold, dividing the histogram into two classes and thus separating the particles (orange) from the background (blue). The algorithm then returns the image as a matrix of 1 (pixels belonging to particles) and 0 (pixels belonging to the background).

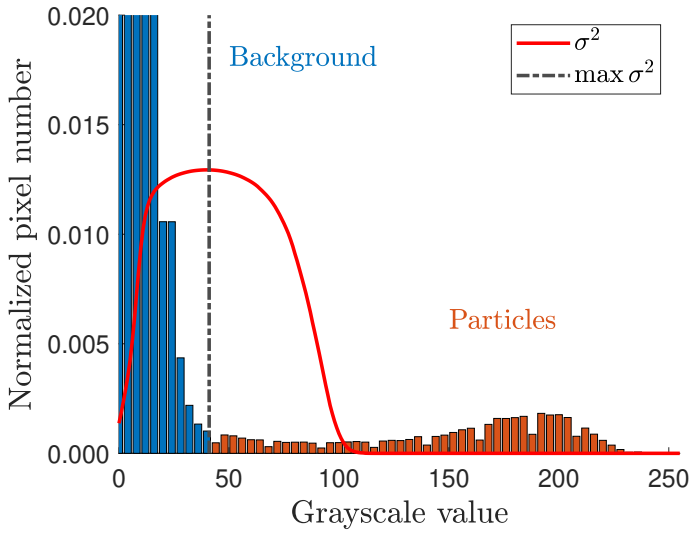

Figure 2: Results of the Otsu algorithm applied to the initial image (Figure 3a) after background subtraction, and the two resulting classes (particles vs background).

It has to be noted that we consider images with good contrast, meaning the particles can be well distinguished from the background. This feature can be observed on the histogram in Figure 2, with many low-value (black) pixels belonging to the background and some high-value (white) pixels belonging to the particles. To obtain such images experimentally, we give special attention to the lighting for good light homogeneity and to prevent light scattering. It facilitates particle detection and results in a more robust procedure. In addition, this limits thresholding issues. Finally, the algorithm detects objects in contact with the frame of the image (that is, any object with a non-zero pixel touching the edge of the image) and erases them; it is done to avoid any misrepresentation of the granulometry or number of particles that are cropped.

Cluster detection. The clustering step detects and isolates clusters in another image and then processes them separately to save computing time. The detection rests upon two criteria: size and eccentricity thresholds. First, it is assumed that the size of a cluster is significantly larger than the mean size of the objects on the current frame. Then, all the objects are analysed as an ellipse with an eccentricity. It is the ratio of the distance between the foci and the major axis length. If the eccentricity is larger than zero, it is a cluster (since an isolated particle is spherical, thus with zero eccentricity). There needs to be more than one criterion to identify clusters correctly. Figures 4a and 4b show a magnification of Figure 3b. One can see the presence of clusters. The red squares refer to the detected objects as clusters. One can note that in Figure 4a, the first criterion selects some isolated particles (in the top left corner, for

instance). Thus the first criterion alone is not optimal. In Figure 4b, the isolated particles are deselected: the two criteria combination allows the sole selection of the clusters.

Watershed. The watershed transform enables detecting particles within a cluster by identifying regions with high- and low-intensity value pixels using a distance transform of the image to segment the objects (Gonzalez and Woods, 2007). Figure 5a displays the clusters selected at the previous step, with a distance transform applied. It shows the distance between a pixel and the nearest nonzero pixel of the binary image. Figure 5b is the second step of the watershed transform and shows the complement of the distance transform. It displays high-elevation in light pixels and low-elevation in dark ones that the watershed transform will use. Finally, Figure 5c displays the resulting particle segmentation: one can see that all the particles within a cluster have different colours, which shows that they have been segmented. Figure 6 displays the particle size distribution before (blue), and after (red) the watershed transform. Before the watershed procedure, the proportion of large particles is much higher than after the watershed treatment. In addition, the experiments were conducted with a particle fraction of diameter between approximately 20 and 30 µm. One can see that the blue curve is out of range of this fraction compared to the one after the watershed treatment. For the given example of Figure 3a, the total particle number is 189, the cluster number is 26, and the particles within the clusters are 50. It shows the importance of this process, as the clusters could misrepresent the results in terms of particle number and granulometry.

Reconstruction. The reconstruction recreates the frame with the isolated particles and the new particles detected within the clusters. It also provides the total particle number.

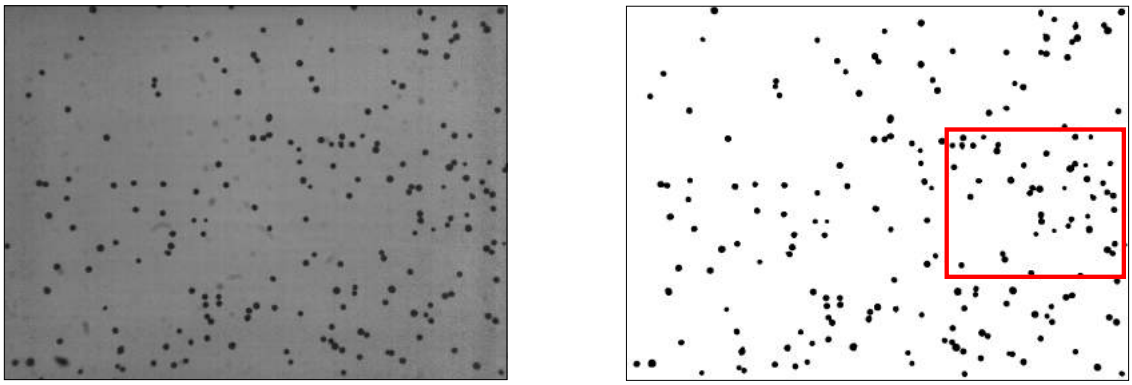

(a) (b)

Figure 3: Image returned by the algorithm for the different processing steps: (a) example of a raw image that is the input of the algorithm (size of 2.0×1.5 mm^2); (b) binary image after the thresholding step. The red frame shows the magnified area for the figures 4 and 5.

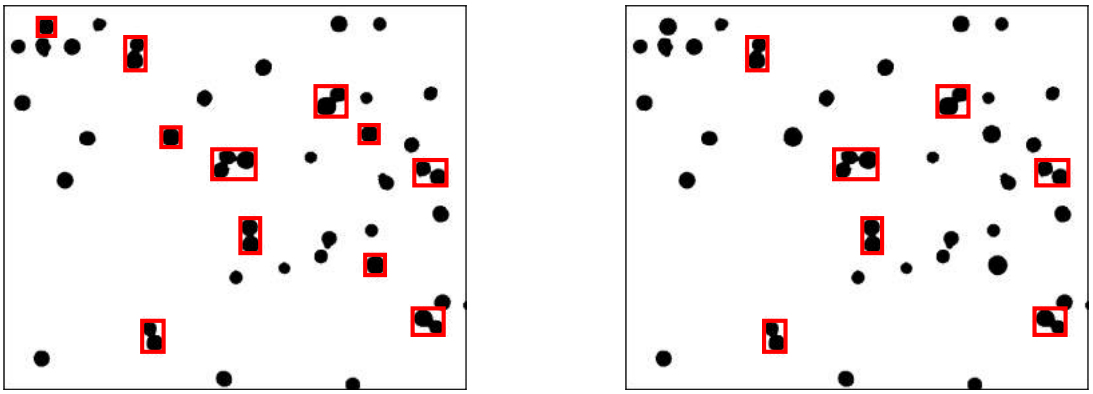

(a) (b)

Figure 4: Magnifications of the images returned by the cluster detection routine after the two detection criteria (size of 818×680 pxl^2): (a) criterion based on the particle size only; (b) criterion based on particle size and on the eccentricity.

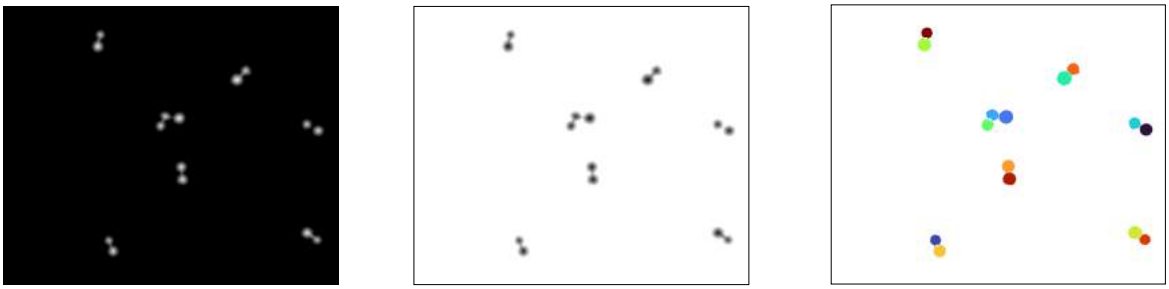

(a) (b) (c)

Figure 5: Magnifications of the images returned by the watershed routine (size of 818×680 pxl^2): (a) distance transform of the complement of the binary image; (b) complement of the distance transform; (c) final image with separated particles, shown in colour for ease of viewing.

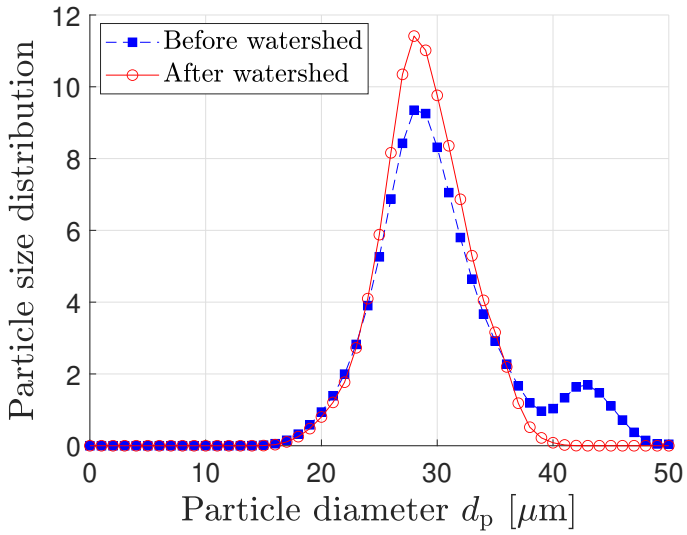

Figure 6: Particle size distribution before and after the watershed treatment.

3. Materials and methods

3.1. Experimental rig

The acquisitions of the temporal evolution of the remaining fraction (see Equation 1) are made within an instrumented open-return wind tunnel resembling a ventilation duct that consists of a 200 cm length rectangular channel flow with a cross-section of 20× 4cm^2 (see Theron et al., 2020). The inlet section comprises an absolute filter followed by a contraction section for flow homogenisation. The channel is made of fully transparent poly(methyl methacrylate). The test area is located 130 cm from the entrance in the rectilineal part to ensure fully developed turbulence. It is made of a glass section which is relatively smooth with a mean roughness of 0.3 nm and a standard deviation of 0.1 nm evaluated by Atomic Force Microscopy (AFM) measurements. The airflow is made by suction, and the fan - located at the outlet - is speed and acceleration controlled. The temperature and relative humidity are measured using a k-type thermocouple and relative humidity sensor of 1.5 °C and 2 % accuracy, respectively. Flow velocity measurements are conducted using a Constant Thermal Anemometry (CTA) acquisition chain (Dantec). It employs a straight miniature wire probe (55P11, Dantec) mounted on elbowed support to acquire the centre velocity U_0 and a hot film glue-on probe (55R47, Dantec) to obtain the wall shear stress on the surface. The experiments consist of depositing particles on the glass surface and then accelerating the air at a mean acceleration α until steady-state is reached. During this transient regime, the deposit is filmed and the airflow properties are acquired.

Particles used in this study come from a fine powder of bronze particles selected for their spherical morphology. Particle sizes affect the resuspension phenomenon. Thus, the raw powder is sieved to tighten the size distribution, separating the initial particle size distribution into size ranges. This study provides results for the [20-30] µm size range, with d_{10} = 19.1 µm, d_{50} = 23.3 µm and d_{90} = 28.9 µm (measured using the particle size analyser Mastersizer 3000 from Malvern Panalytical). The microparticles are deposited on the surface by gravity using a particle generator and a sedimentation chamber. One can calculate the sedimentation time t_{sed} as a function of the chamber height h and the particle diameter d_p: the larger the particle diameter, the smaller the sedimentation time. Limiting the duration of the sedimentation process ensures that the largest particles are deposited while the least amount of small particles reaches the surface. Consequently, the size distribution obtained for the particle at the surface differs from that obtained from the size analyser, shifting towards larger sizes and narrowing the distribution.

The image measurements are carried out with a CCD camera (SpeedSense 1020, Dantec) and an optical zoom x12 (LaVision) placed underneath the deposition surface. The camera is combined with a LED panel of 50 W power, directed through the measurement area onto a camera in the same manner as for shadow PIV setups. The field of view is 2.0 × 1.5 mm^2 and placed at the beginning of the deposit (in the streamwise direction) to ensure a minimal

collision number. It corresponds to a CCD sensor size of 2320×1728 pixels^2; each pixel size is thus 0.86 µm. Thus, the particles size range [20-30] µm corresponds to [23-35] pixels. The camera is refocused on the particles just before the acquisition, and the led panel is switched on. The background image is obtained at the end of a measurement after cleaning the surface to remove any remaining particles. We show an example of a raw image (Figure 7a), the resulting image after background subtraction (Figure 7c), and its corresponding grayscale value histogram (Figure 7e).

A trigger synchronises the fan ignition, the camera and the StreamLine system for the hot wire and film probe acquisitions. For the camera, it is linked to a signal generator (Sony Tektronix AFG310) which produces a square wave signal at a given frequency setting the image acquisition off. The acquisition frequency is set at 30 Hz to have the best compromise between image quality and brightness. Regardless of the condition, each data acquisition lasts for 85 s, corresponding to the ratio of the maximum buffer size and the acquisition frequency.

3.2. Synthetic data

Synthetic images are created by randomly adding spherical dots to a background obtained experimentally, as described previously. As the algorithm erases the particles at the border, a constraint is added at the generation to prevent an object from being in contact with the edge of the images. Thus, the images contain only whole particles that ought to be detected by the algorithm. The particle concentration is of the same magnitude order as that found experimentally. The size of the synthesised particles is randomly chosen from a Gaussian distribution (the same distribution found experimentally). Then, the routine adds noises to the image:

- Gaussian noise that one typically encounters in image acquisition procedure due to the stochastic procedure of photo-counting and intrinsic thermal and electronic fluctuations of devices (Luisier et al., 2011; Boyat and Joshi, 2015);
- "salt and pepper" noise that may arise due to channel transmission (Charbit and Blanchet, 2014).

We generate one thousand images using this procedure. The background image used by the algorithm is calculated as the mean image of all the synthetic images. This procedure is performed to generate a background image that is different from the one used when creating the synthetic images (otherwise, the successive background addition subtraction would be pointless) and to further test our algorithm's robustness. We show an example of a synthetic image created with $N_\mathrm{p} = 250$ particles and particle diameter distribution parameters with a mean value of $\mu = 25$ µm and a standard deviation value of $\sigma = [3, 5]$ µm^2 in Figure 7b. One can see the resulting image after background subtraction (Figure 7d) and its corresponding grayscale value histogram (Figure 7f).

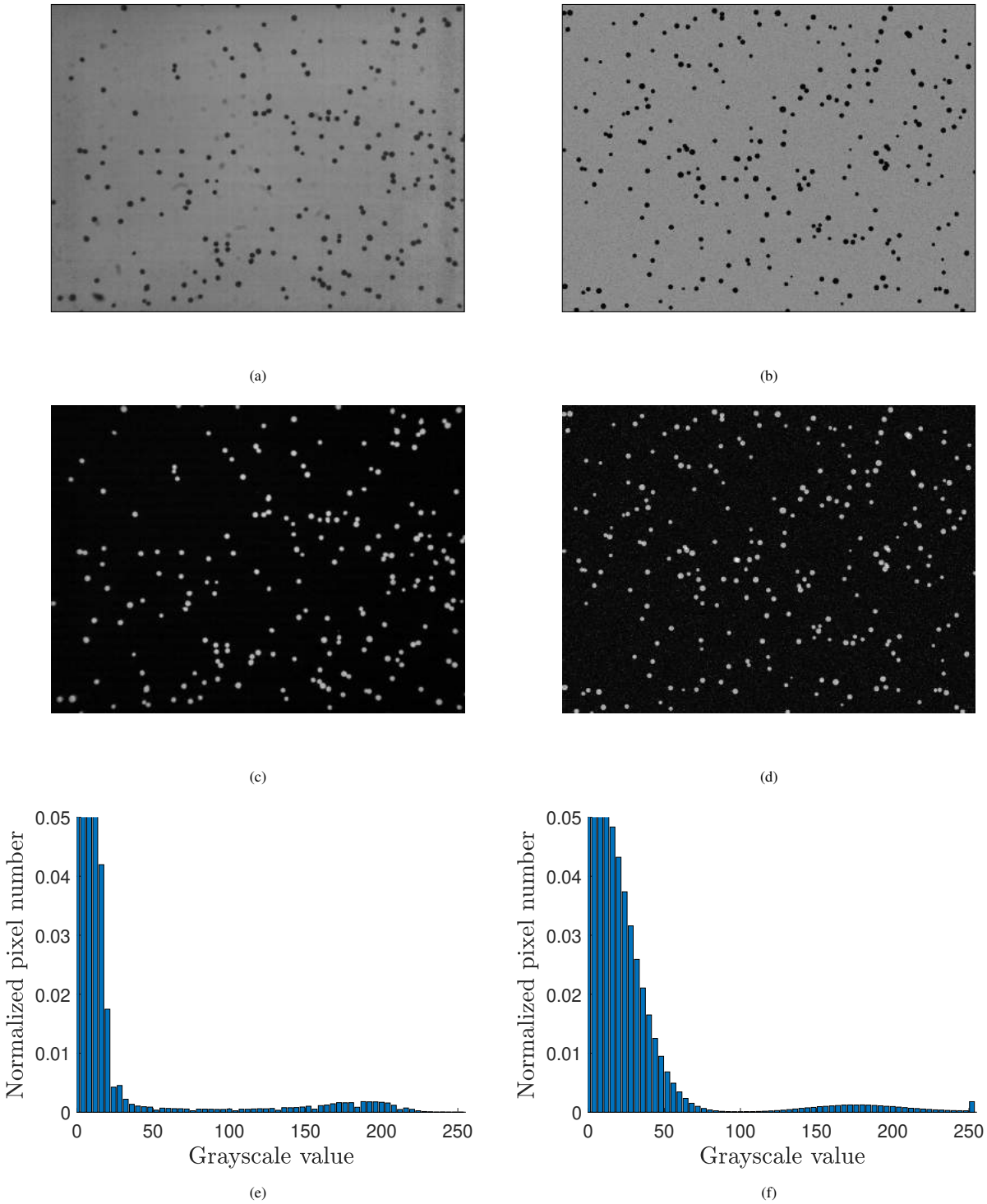

Figure 7: (a) Raw image obtained from an experimental acquisition, of size 2.0×1.5 mm^2; (b) synthetic image created by the algorithm with $N_\mathrm{p} = 250$ particles and distribution parameters of $\mu = 25$ µm and $\sigma = [3, 5]$ µm^2, with the same pixel size as the raw image (2320×1728 pxl^2); (c) raw image after background subtraction; (d) synthetic image after background subtraction; (e) normalised grayscale value histogram of the raw image after background subtraction; (f) normalised grayscale value histogram of the synthetic image after background subtraction.

4. Results and discussion

4.1. Algorithm validation on synthetic data

The algorithm's reliability was tested by generating a synthetic image with known parameters and then applying the detection algorithm to it in order to compare the particle number and the size distribution.

First, the particle numbers are compared between the initial parameter and the returned number by the algorithm. The convergences of the mean and the variance of the relative differences $N_\epsilon = (N_\mathrm{p} - N)/N_\mathrm{p}$ (with N the particle number returned by the algorithm) are calculated for an increasing image number from 1 to 1000, with the following parameters: $N_\mathrm{p} = 250$ particles, $\mu = 25$ µm and $\sigma = [3, 5]$ µm^2. Figure 8a indicates the statistical convergence of the mean and variance of the relative difference as a function of the number of images used. One can see some oscillations for low values of images used, then the convergence at approximately 700 images. Thus, we choose a sample length of 1000 for the validation to ensure statistical convergence.

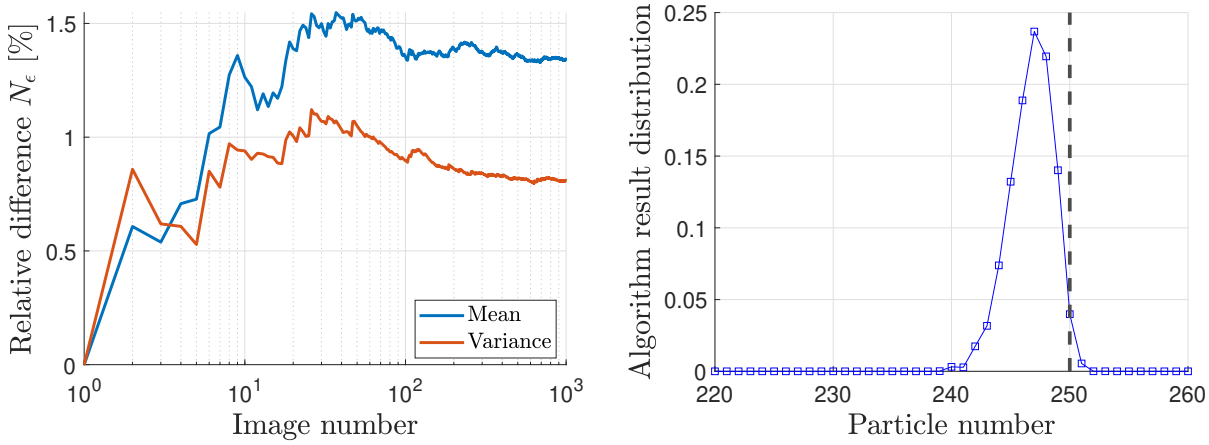

(a) (b)

Figure 8: (a) convergence of the mean and the variance of the relative difference N_ϵ between initial and final particle numbers as a function of the number of images used; (b) distribution of the particle number returned by the algorithm for 1000 images with the initial particle number N_p (black dashed line). In both figures, the synthetic image parameters are $N_\mathrm{p} = 250$ particles, $\mu = 25$ µm and $\sigma = [3, 5]$ µm^2.

The validation routine generates 1000 synthetic frames for different size distribution parameters (mean and variance). For fixed parameters, all the images have the same particle concentration. The algorithm processes all these frames and returns the size distribution and the particle numbers to compare them with the initial distribution and particle number. As the particle positions are random, clusters may exist on the image; the clustering and watershed routines are therefore tested in this validation.

Figure 8b displays an example of the counting for 1000 images and the parameters $N_\mathrm{p} = 250$ particles, $\mu = 25$ µm and $\sigma = [3, 5]$ µm^2. The black dashed line is the actual particle number, and the distribution represents the numbers returned by the algorithm. This distribution points out a bias and a variance. The presence of clusters and particles in contact with the image frame cause them. Indeed, there is no condition on the generation of particles on the synthetic image: particles may overlap. Thus, it potentially produces two errors: the cluster detection routine will not detect objects as clusters, and if it is detected the watershed routine will not segment well the particles. As a result, the algorithm underestimates the particle number or it may create 'fake' particles.

Then, the granulometry between the synthetic image and the result from the algorithm is compared using the Bhattacharyya distance. It is defined as the measure of the similarity between two discrete probabilities $p(x)$ and $q(x)$ for x, a random variable (Bi et al., 2019) and is used to compare two distributions. One can compute it using (Bhattacharyya, 1946):

$$D_\mathrm{B}(p, q) = -\ln\left(BC(p, q)\right), \tag{2}$$

where BC is the Bhattacharyya coefficient defined as

$$BC(p,q) = \sum_{x \in X} \sqrt{p(x)q(x)}, \tag{3}$$

As expected, the closer D_B is to zero, the more similar the two distributions are. One can see the Bhattacharyya distance as a similarity measurement between two distributions. Figure 9 shows an example of the initial and final particle size distribution for the same parameters as before. In this example, x is the particle diameter d_p and p and q are the probability distribution before and after the algorithm treatment. It also displays the Bhattacharyya distance of $D_B = 0.21$ %. The distributions are very similar, which explains the low values of the Bhattacharyya distances.

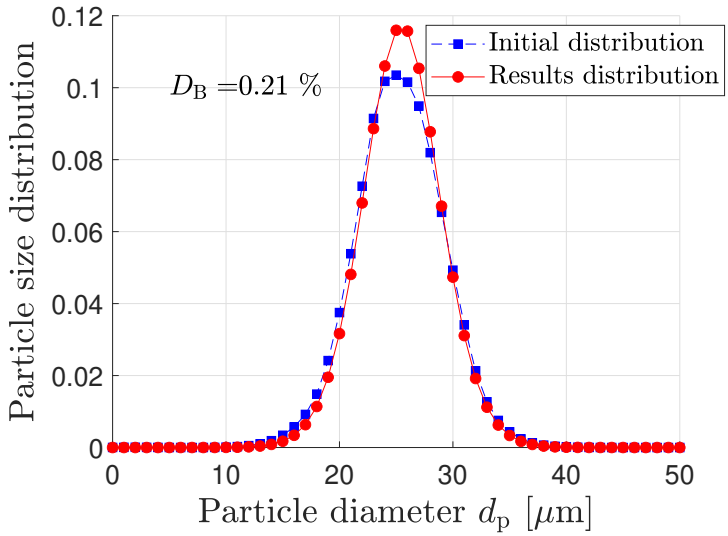

Figure 9: Particle size distributions of the synthetic image (blue square) and the algorithm result (red circle) with the corresponding Bhattacharyya distance D_B.

Table 1 displays the results for different initial particle numbers N and parameters μ and σ for the initial particle size distribution. The results show mean and standard deviation values because the routine computes the particle number relative differences and the Bhattacharyya distances for 1000 images for each condition. The Bhattacharyya distance values expressed in percentage are very close to zero, reflecting that the particle size distributions before and after the process are very close. It can be concluded that the sizes returned by the algorithm are very close to the true particle size and that the loss of information during the restoration and binarisation processes is negligible.

	N = 150		N = 300	
	μ=15, σ=[3,5]	μ=25, σ=[4,5]	μ=15, σ=[3,5]	μ=25, σ=[4,5]
$N_{\epsilon,\text{mean}}$ [%]	0.61	0.9	1.4	1.8
$N_{\epsilon,\text{std}}$ [%]	0.6	0.8	0.6	0.8
$D_{B,\text{mean}}$ [%]	0.36	0.39	0.27	0.33
$D_{B,\text{std}}$ [%]	0.15	0.15	0.11	0.12

Table 1: Comparison between the relative difference ϵ between the initial and final particle number and the initial particle size distribution and the one returned by the algorithm using the Bhattacharyya distance D_B. N is the initial particle number, and μ and σ are the mean and variance of the normal distribution used for the synthetic image creation, respectively.

Finally, the same procedure was conducted for an extensive range of numbers of particles N_p and particle size mean diameters μ. Figure 10 displays the mean of the relative difference N_ϵ as a function of N_p for different μ values. As the μ value increases, the error grows, and for any given μ value, the mean relative difference increases with the

particle number. One can also see that the slope increases with μ. It is due to the watershed procedure; larger particles are more inclined to form clusters and overlap for the same window size. For the particle number comparison, the more particles there are, the less accurate the algorithm is. It is due to the increase of the number of clusters with the particle concentration.
Furthermore, this effect intensifies with the mean particle diameter μ. We tested the algorithm for 1000 and 1500 particles per image with mean particle diameter $\mu = 15$ µm and $\mu = 40$ µm (not shown in this paper). While N_ϵ stays below 7 % for the smallest diameter, it reaches 45 % to 80 % for the largest one.

Nevertheless, the difference between the initial particle number and the number returned by the algorithm stays below $\epsilon = 3$ % for the experimental conditions mentioned above, especially in the limit of 300 particles per image. Thus, we validate the count of the algorithm for processing the synthetic data.

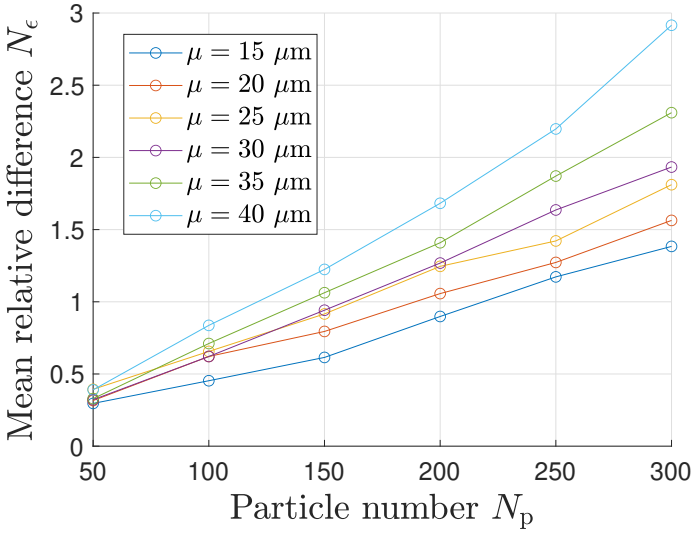

Figure 10: Mean of the relative difference N_ϵ for six initial particle numbers N_p and six mean values of the particle size distribution μ, for $\sigma = [3, 5]$ µm^2.

4.2. Algorithm validation on experimental data

The second validation consists of a manual particle count in both the first and last images of the movies and comparing them with the algorithm results. In this validation, human eye counting is considered the accurate result, even though errors may remain. Note that manual counts were also performed on the synthetic images and yields a relative difference of 0 % on the results. Like in the algorithm, the user does not count a particle when the frame of the image crops it. We validate the algorithm manually using 20 acquisitions (40 images). The mean values of the relative differences between the human counting and the algorithm result are 2.14 % and 2.17 % for the initial and final images, respectively. The respective standard deviations are 0.009 and 0.015. These values are low as they remain below 3 % with relatively low standard deviation values. Thus, it is assumed that the algorithm is close to the actual particle number.

Numerical and experimental procedure validates the algorithm: it gives a particle number close to reality and returns the correct particle size. Therefore, one can use it to perform post-processing on experimental data.

4.3. Deposit properties

The first frame of each movie gives insights into the initial deposit. It allows visual and quantitative validation for experimental acceptance in terms of concentration, homogeneity, and particle size distribution. After detecting the particle number, the algorithm investigates the particle concentration by dividing the particle number by the field of view area. In addition, it returns the granulometry of the deposit by analysing all the particle sizes. An example

of a particle size distribution is presented in Figure 11 for 192 particles, i.e., a concentration of 64 particles.mm^{-2}. One can remark that the distribution is slightly different from the distribution returned by the Malvern. There are two reasons: the deposition process is designed for and 1-D calibration for the resolution. Any further analysis linked with particle size should address the calibration issue. Nevertheless, all the further results will use the particle distribution given in Figure 11 as a reference.

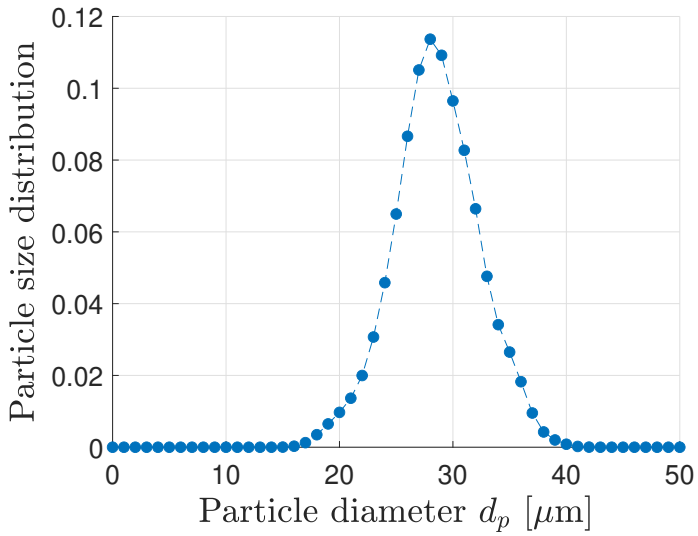

Figure 11: Normalised particle size distribution of the image of Figure 7a.

Since this study on particle resuspension concerns mono-layer deposits of isolated particles, it is also interesting to investigate the deposit homogeneity in terms of its spatial distribution. To this end, the algorithm uses Voronoï diagrams to study the deposit homogeneity based on the work of Fiabane et al. (2012) and references therein. This algorithm segments the images from seeds - corresponding to the centres of the particles - into Voronoï cells; these cells are defined by the points in the plane closest to their respective seed. Then the distribution of Voronoï cell areas is computed and compared to a Gamma function similar to a random Poisson distribution. The closer the distribution is to the Gamma distribution, the more random the cell size distribution. Such a random cell size distribution can be linked to the randomly distributed deposition of particles on the whole area of interest, with no significant clusters of particles in some parts and wide empty areas in others. This random distribution is, therefore, what we regard as a homogeneous deposit. Figure 12a provides an example of a Voronoï segmentation on an experimental dataset, and the resulting area distribution is compared to a Gamma distribution in Figure 12b. As one can observe, the experimental result is very close to that of a random distribution, meaning that the initial deposit is spatially homogeneous.

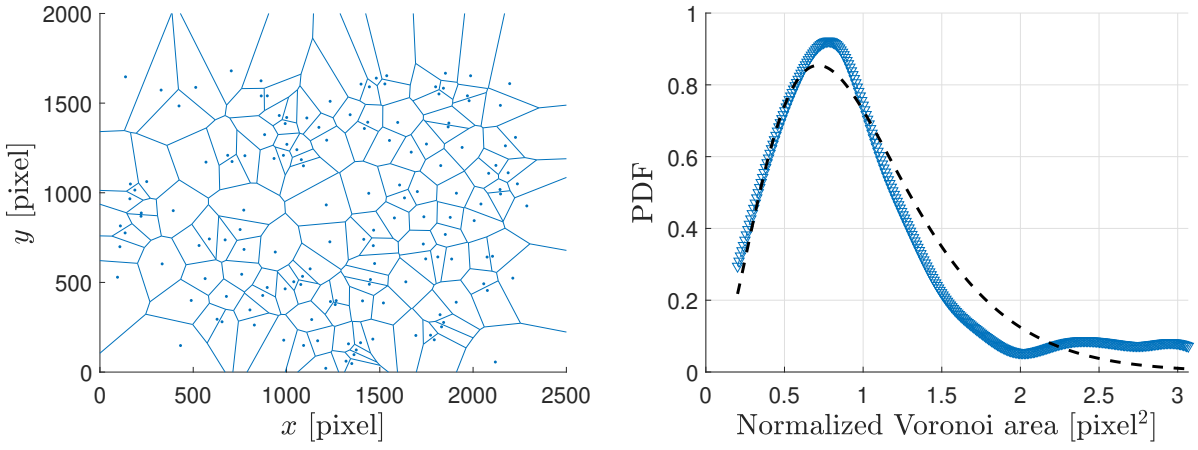

(a) (b)

Figure 12: Voronoï treatment based on the image of Figure 3a: (a) Voronoï tessellation of the image, the dots represent the particle centres, and the lines delimit the Voronoï areas; (b) superimposition of the resulting normalised Voronoï area Probability Density Function (PDF) (blue dots) and Gamma distribution (black dashed line).

Combining the size and spatial distribution results, one can conclude that the deposition procedure is valid: it creates a homogeneous mono-layer deposit of a relatively narrow particle diameter range.

4.4. Temporal evolution of the particle number

One of the algorithm's main features is the ability to track the particle number automatically, thus the time evolution of the remaining particle on the surface. Figure 13a represents the evolution of the particle number for the airflow properties $U_0 = 9.0\ \mathrm{m\,s^{-1}}$ and $\alpha = 2.1\ \mathrm{m\,s^{-2}}$ for seven trials. Each trial consists of a new deposit acquisition. We ensure that all the particle size distributions of the deposits are similar. The initial particle numbers $N_{\mathrm{p,init}}$ range from 142 to 229. Figure 13b presents the evolution of the remaining fraction of particles on the surface over time computed using equation 1. The algorithm sums the particles for all acquisitions (Figure 13a) for a temporal velocity profile to be statistically representative.

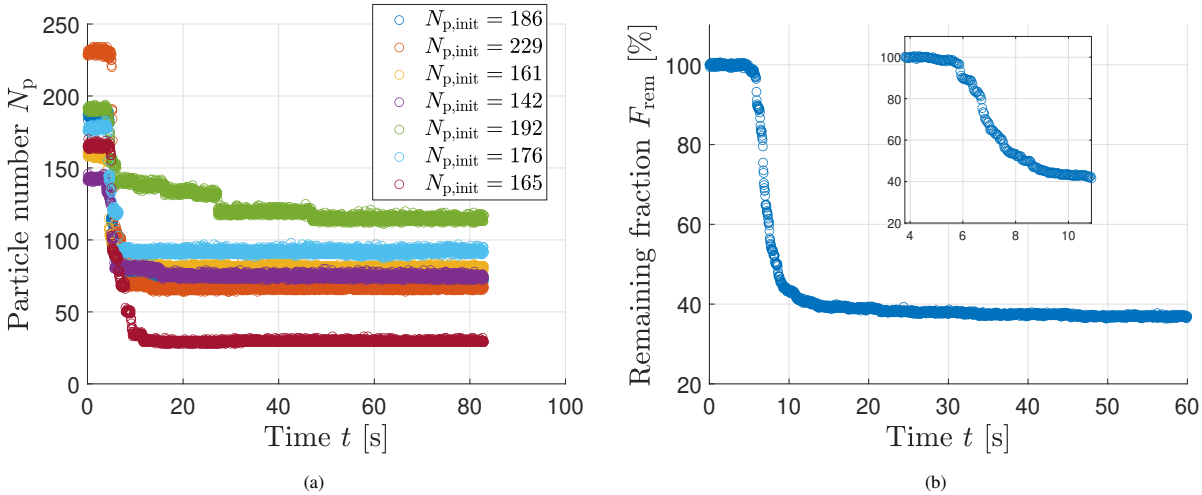

(a) (b)

Figure 13: Example of acquisition results for the airflow conditions $U_0 = 9.0\ \mathrm{m.s^{-1}}$ and $\alpha = 2.1\ \mathrm{m.s^{-2}}$: (a) particle number over time for seven trials at the same conditions; (b) remaining fraction of particles on the duct surface as a function of time, representing the average over the data of (a). Insert represents a magnification of the area where most of particles are resuspended.

As expected, the percentage of remaining particles drops from 100 % to a plateau, here at approximately 39 % (see Figure 13b). It corresponds to the initial deposition before exposing it to the airflow and at the end of the experiment. It represents a cumulative number of 1251 and 391 particles, respectively, over the seven trials. One can see the presence of fluctuations on the remaining fraction curve. They are due to existing vibrations in the channel flow during experiments. As a result, the particles move slightly relative to the camera frame of reference from one image to another, and the detected size by the algorithm may vary. As the criteria for cluster identification is size threshold based, the same object may not be detected within two consecutive time steps. Therefore, it can be analysed as a single particle or particle cluster.

As aforementioned, the influence of particle size on the resuspension phenomenon can be studied by the algorithm. The algorithm follows the evolution of the granulometry over time. One can compare the granulometry distributions at different times to reveal features such as particle sizes that are preferentially resuspended. Figure 14 shows an example of the granulometry at the beginning (blue curve) and at the end (red curve) of an acquisition. Note that this result is obtained after the watershed treatment and each particle is treated individually; thus, larger diameters in Figure 14 correspond to larger particles and not to clusters. For these experiments, the aerodynamic properties are $U_0 = 7.6\ \mathrm{m\,s^{-1}}$ and $\alpha = 0.3\ \mathrm{m\,s^{-2}}$ with 141 and 69 particles at the beginning and at the end, respectively. The distribution is multimodal, with three modes. At the end of the acquisition, the highest value mode disappears; the ratio between the first mode and the second mode values increases; thus, there are more small particles in proportion on the surface. One concludes that large particles are more prone to detach than small ones, in agreement with the experimental literature (Ibrahim et al., 2003; Kassab et al., 2013; Vincent et al., 2019). We suspect that collisions may play an additional role in these results: our particle concentration is substantially larger than that of other papers, leading to larger probabilities of collision and resuspension especially for large particles.

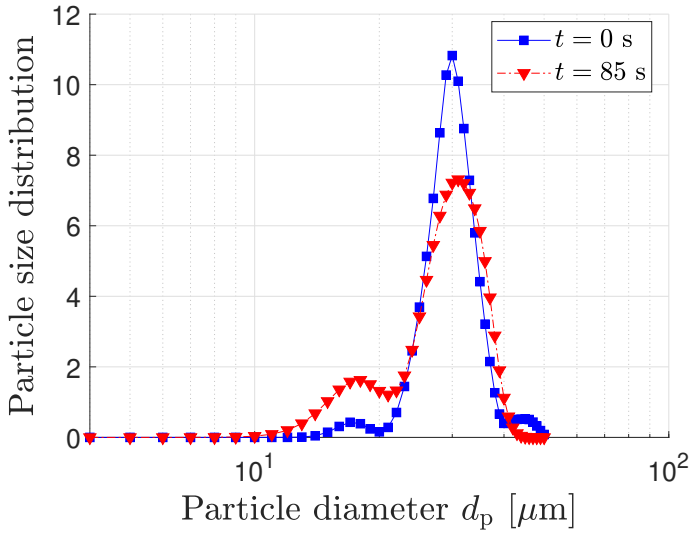

Figure 14: Probability density function of the particle diameters d_p at the beginning and the end of acquisition for the velocity parameters $U_0 = 7.6\ \mathrm{m\,s^{-1}}$ and $\alpha = 0.3\ \mathrm{m\,s^{-2}}$.

Moreover, the algorithm can discriminate particles according to their sizes. It means that for the same acquisition, it is also possible to see preferentially resuspended particle fractions by tracking the particle number evolution over time. Figure 15 gives an example of the remaining fraction over time for particle diameter less and larger than 30 µm in blue and red, respectively. We chose this particle size threshold as the principal mode of the particle size distribution of the deposit returned by the algorithm. The initial and final particle numbers are 116 and 26, respectively, for the blue curve, and 53, 9 for the orange curve. One can see that the orange curve is below the blue one at the end of the experiment. Larger particles seem to resuspend easier than smaller ones, as seen above.

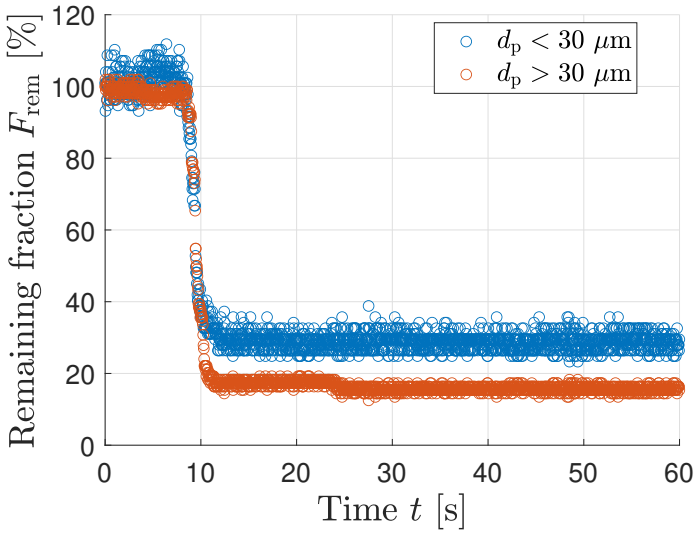

Figure 15: Remaining particle fraction over time for two particle size range for the same acquisition with velocity parameters $U_0 = 10.0\ \mathrm{m\,s^{-1}}$ and $\alpha = 1.0\ \mathrm{m\,s^{-2}}$.

The dynamics of the resuspension phenomenon seems to occur in a short time (see Figure 13b), namely in the transient regime when the flow accelerates. Drawing a link between the particles resuspension and the airflow properties, such as the friction velocity or the flow features, might help understand the process. It will be the subject of further studies with the help of the present algorithm.

4.5. Cluster identification

As the algorithm can detect clusters, it is interesting to use this property to evaluate their behaviour and the particles inside them after the watershed transform. The resuspension process involves collisions (Rondeau et al., 2021), and one can assume that clusters are more subject to this phenomenon due to their larger size. Therefore, it could be interesting to track their behaviour during the resuspension stage to study the influence of the presence of clusters. Figure 16 provides a graph showing the total particle evolution, clusters, and particles in cluster numbers over time. One can look over the cluster behaviour during the transient regime. So far, our study found no particular transient trend or pattern for the acquisition frequency employed for all the aerodynamic conditions tested.

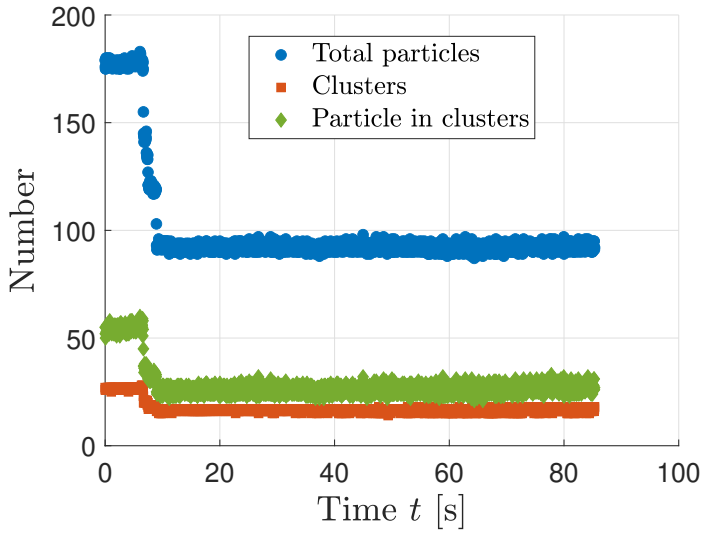

Figure 16: Evolution of the number of total particles, clusters, and particles in clusters in time during an experiment.

4.6. Known limits

Although we are confident in the results obtained using the presented algorithm, one has to be aware of some limits identified during our different tests. First, the particle detection algorithm relies on the particles being spherical, with a corresponding round-shaped object on the images. Therefore, one can apply the algorithm to other experimental datasets to detect particles as long as the particles are spherical. Otherwise, the cluster detection routine might detect them as clusters, as it is based on the spherical property of particles (mean size and eccentricity of an ellipse). Nevertheless, this difficulty might be overcome by tuning the criteria using suitable geometric properties for both particle and cluster detection; it would be helpful for other applications, such as fibre resuspension (Capone et al., 2021).

Second, it has to be noted that the particle size distribution results depend on the resolution calibration. In our experiments, we calibrate using a one-dimensional calibration target (stage micrometre), assuming that the camera and the surface are perfectly aligned. We are working on a two-dimensional calibration to ensure better accuracy and position-dependent resolution. Moreover, as mentioned previously, the whole experimental setup must be thought carefully to acquire the best image possible with good contrast between the background and the particles. We have not tested the algorithm's limits when degrading the raw image quality.

Third, the algorithm is relatively fast ($\sim$ 1 second per frame) for these acquisitions. However, for higher acquisition rates, the time processing would be too long ($\sim$ 16 hours for an acquisition frequency of 1 kHz during 60 seconds). An evaluation of function computation times provided in Table 2 for one frame shows that the watershed transform represents 88 % of computational time. Thus, efforts must be made to help reduce this computation time by optimising it. For instance, the algorithm could decompose an image into subsets to process each sub-frame simultaneously on a parallelised watershed routine.

Function	Binarise	Clustering	Watershed	Recompose
Time [s]	0.087	0.045	1.051	0.010
Fraction [%]	7.3	3.8	88.1	0.8

Table 2: Computation times of each function for one image treatment, along with their respective fraction.

Finally, one limit emerged more with the study subject than with the algorithm. The flow of interest is an accelerated flow from rest to a steady state. As such, it yields faster events: faster particle velocities when set in motion as well as stronger particle velocity gradient, more energetic shocks between particles with faster velocities after impact, etc. One needs to have a higher acquisition frequency with a faster flow to capture all these events on sharp and

contrasted images. Consequently, in many cases, the frequency used for the image acquisition becomes too low after a certain velocity: one can not follow some characteristic behaviour of particle resuspension (e.g. particle velocity and velocity gradient or collision). Moreover, the faster particles might leave a blurry mark on the image instead of a round-shaped object, adding noise and conflicting with the detection algorithm. It is possible to partially resolve this issue by setting the acquisition frequency of the whole sequence at the maximum needed value. Several strategies can be considered: simply increasing the acquisition frequency of the camera, decreasing the image resolution to make a further frequency increase possible, or changing the camera to a faster one. Either way, all these solutions come with two additional issues: the need for more powerful lighting and more extensive sequences of images to post-treat. At last, the fan induces vibrations on the channel. Consequently, it adds noise to the images and affects the algorithm processing as the cluster detection. A first step to avoid any external disturbance was made by separating the fan from the support structure of the channel. Nevertheless, some vibrations remain. Other methods should be added, such as ballast of the channel or anti-vibration pads.

5. Conclusions

In this paper, we have proposed an algorithm to study the microparticle resuspension phenomenon. The deposits are initially mono-layers, composed of isolated microparticles between 20 and 30 µm. They are subject to airflow acceleration followed by steady-state. The automatic algorithm makes it possible to obtain the microparticle number evolution over time and other parameters which characterise the deposits, like granulometry or homogeneity. Finally, it detects the presence of particle clusters. It identifies the particles inside them to have a more reliable count and to track the temporal evolution of these objects. It is validated using two methods. The synthetic method measures the bias of the count, less than 4 %, and its variance, less than 2 %. The manual method measures an error below 3 %.

The algorithm opens up opportunities to study resuspension dynamically. The literature lacks combined remaining fractions with flow properties during the transitional regime. This algorithm enables automatic particle detection on a film with a high-frequency acquisition. One must note that the algorithm is not reduced to the application of this paper, but one can process movies with higher acquisition rates to detect other behaviours. One can link the remaining particle fraction with the airflow properties, such as the centre velocity, friction velocity and their respective fluctuations, and the resulting turbulent kinetic energy. The possible correlations between these parameters and the remaining fraction evolution could provide knowledge on the resuspension phenomenon.

The algorithm detects the presence of clusters and processes them separately and the particle within these clusters. One will be able to learn more about their involvement in resuspension, their role in collisions, and the different resuspension scenarios described in the models of Guingo and Minier (2008) or Henry and Minier (2014b). Moreover, the algorithm discriminates particles based on their size. Thus, one can study the influence of this parameter on the resuspension to improve other models (Chatoutsidou et al., 2017).

Declaration of competing interest

The authors declare that they have no known competing financial interests or personal relationships that could have appeared to influence the work reported in this paper.

Data availability

The algorithms and data are available online: Cazes et al. (2023) and CAZES et al. (2023), respectively. For the purpose of Open Access, a CC-BY public copyright licence has been applied by the authors to the present document and will be applied to all subsequent versions up to the Author Accepted Manuscript arising from this submission.

Acknowledgements

This work is financially supported by the French Ministry of the Armed Forces - Defence Innovation Agency and the Pays de la Loire Region, France. We gratefully acknowledge the support of Institut des Matériaux de Nantes (IMN) for the AFM measurements.

References

Agüí, J.C., Jiménez, J., 1987. On the performance of particle tracking. Journal of Fluid Mechanics 185, 447–468. doi:https://doi.org/10.1017/S0022112087003252.

Barth, T., Preuß, J., Müller, G., Hampel, U., 2014. Single particle resuspension experiments in turbulent channel flows. Journal of Aerosol Science 71, 40–51. doi:https://doi.org/10.1016/j.jaerosci.2014.01.006.

Benito, J., Aracena, K., Uñac, R., Vidales, A., Ippolito, I., 2015. Monte Carlo modelling of particle resuspension on a flat surface. Journal of Aerosol Science 79, 126–139. doi:https://doi.org/10.1016/j.jaerosci.2014.10.006.

Bhattacharyya, A., 1946. On a Measure of Divergence between Two Multinomial Populations. Sankhyā: The Indian Journal of Statistics 7, 401–406.

Bi, S., Broggi, M., Beer, M., 2019. The role of the Bhattacharyya distance in stochastic model updating. Mechanical Systems and Signal Processing 117, 437–452. doi:https://doi.org/doi.org/10.1016/j.ymssp.2018.08.017.

Boyat, A.K., Joshi, B.K., 2015. A Review Paper : Noise Models in Digital Image Processing. Signal & Image Processing : An International Journal 6, 63–75. doi:https://doi.org/10.5121/sipij.2015.6206.

Braaten, D.A., 1994. Wind Tunnel Experiments of Large Particle Reentrainment-Deposition and Development of Large Particle Scaling Parameters. Aerosol Science and Technology 21, 157–169. doi:https://doi.org/10.1080/02786829408959705.

Canny, J., 1986. A Computational Approach to Edge Detection. IEEE Transactions on Pattern Analysis and Machine Intelligence PAMI-8, 679–698. doi:https://doi.org/10.1109/TPAMI.1986.4767851.

Capone, A., Di Felice, F., Alves Pereira, F., 2021. Flow-Particle Coupling in a Channel Flow Laden with Elongated Particles: The Role of Aspect Ratio. Journal of Marine Science and Engineering 9, 1388. doi:https://doi.org/10.3390/jmse9121388.

Cazes, C., Fiabane, L., Heitz, D., Théron, F., Le Coq, L., 2023. Automatic particle detection algorithm. URL: `https://hal.inrae.fr/hal-03954927`.

CAZES, C., FIABANE, L., THERON, F., HEITZ, D., LE COQ, L., 2023. Bronze particle resuspension in an accelerated flow. URL: `https://doi.org/10.57745/XHRRXF`, doi:10.57745/XHRRXF.

Charbit, M., Blanchet, G., 2014. Digital Signal and Image Processing using MATLAB. volume 1. ISTE-WILEY.

Chatoutsidou, S.E., Drossinos, Y., Tørseth, K., Lazaridis, M., 2017. Modelling of particle resuspension by a turbulent airflow and the role of particle size, surface roughness and electric charge. Journal of Adhesion Science and Technology 31, 817–843. doi:https://doi.org/10.1080/01694243.2016.1232955.

Crocker, J.C., Grier, D.G., 1996. Methods of Digital Video Microscopy for Colloidal Studies. Journal of Colloid and Interface Science 179, 298–310. doi:https://doi.org/10.1006/jcis.1996.0217.

D'Alicandro, A.C., Massarotti, N., Mauro, A., 2021. Aerosol hazards in operating rooms: A review of numerical and experimental studies. Journal of Aerosol Science 158, 105823. doi:https://doi.org/10.1016/j.jaerosci.2021.105823.

Evangeliou, N., Zibtsev, S., Myroniuk, V., Zhurba, M., Hamburger, T., Stohl, A., Balkanski, Y., Paugam, R., Mousseau, T.A., Møller, A.P., Kireev, S.I., 2016. Resuspension and atmospheric transport of radionuclides due to wildfires near the Chernobyl Nuclear Power Plant in 2015: An impact assessment. Scientific Reports 6, 26062. doi:https://doi.org/10.1038/srep26062.

Fiabane, L., Zimmermann, R., Volk, R., Pinton, J.F., Bourgoin, M., 2012. On the clustering of finite-size particles in turbulence. Physical Review E 86, 5. doi:https://doi.org/10.1103/PhysRevE.86.035301.

Giering, S.L.C., Hosking, B., Briggs, N., Iversen, M.H., 2020. The Interpretation of Particle Size, Shape, and Carbon Flux of Marine Particle Images Is Strongly Affected by the Choice of Particle Detection Algorithm. Frontiers in Marine Science 7, 564. doi:10.3389/fmars.2020.00564.

Goldasteh, I., Ahmadi, G., Ferro, A.R., 2013. Wind tunnel study and numerical simulation of dust particle resuspension from indoor surfaces in turbulent flows. Journal of Adhesion Science and Technology 27, 1563–1579. doi:https://doi.org/10.1080/01694243.2012.747729.

Gonzalez, R.C., Woods, R.E., 2007. Digital Image Processing. 3e ed., Pearson.

Gradoń, L., 2009. Resuspension of particles from surfaces: Technological, environmental and pharmaceutical aspects. Advanced Powder Technology 20, 17–28. doi:https://doi.org/10.1016/j.apt.2008.10.009.

Guingo, M., Minier, J.P., 2008. A new model for the simulation of particle resuspension by turbulent flows based on a stochastic description of wall roughness and adhesion forces. Journal of Aerosol Science 39, 957–973. doi:https://doi.org/10.1016/j.jaerosci.2008.06.007.

Henry, C., Minier, J.P., 2014a. Progress in particle resuspension from rough surfaces by turbulent flows. Progress in Energy and Combustion Science 45, 1–53. doi:https://doi.org/10.1016/j.pecs.2014.06.001.

Henry, C., Minier, J.P., 2014b. A stochastic approach for the simulation of particle resuspension from rough substrates: Model and numerical implementation. Journal of Aerosol Science 77, 168–192. doi:https://doi.org/10.1016/j.jaerosci.2014.08.005.

Ibrahim, A., Dunn, P., 2006. Effects of temporal flow acceleration on the detachment of microparticles from surfaces. Journal of Aerosol Science 37, 1258–1266. doi:https://doi.org/10.1016/j.jaerosci.2006.01.007.

Ibrahim, A., Dunn, P., Brach, R., 2003. Microparticle detachment from surfaces exposed to turbulent air flow: controlled experiments and modeling. Journal of Aerosol Science 34, 765–782. doi:https://doi.org/10.1016/S0021-8502(03)00031-4.

Ibrahim, A., Dunn, P., Brach, R., 2004. Microparticle detachment from surfaces exposed to turbulent air flow: Effects of flow and particle deposition characteristics. Journal of Aerosol Science 35, 805–821. doi:https://doi.org/10.1016/j.jaerosci.2004.01.002.

Jiang, Y., Matsusaka, S., Masuda, H., Qian, Y., 2008. Characterizing the effect of substrate surface roughness on particle–wall interaction with the airflow method. Powder Technology 186, 199–205. doi:https://doi.org/10.1016/j.powtec.2007.11.041.

Kassab, A.S., Ugaz, V.M., King, M.D., Hassan, Y.A., 2013. High Resolution Study of Micrometer Particle Detachment on Different Surfaces. Aerosol Science and Technology 47, 351–360. doi:https://doi.org/10.1080/02786826.2012.752789.

Kottapalli, K., Novosselov, I.V., 2021. Aerodynamic resuspension and contact removal of energetic particles from smooth, rough, and fibrous surfaces. Talanta 231, 122356. doi:https://doi.org/10.1016/j.talanta.2021.122356.

Krauter, P., Biermann, A., 2007. Reaerosolization of Fluidized Spores in Ventilation Systems. Applied and Environmental Microbiology 73, 2165–2172. doi:https://doi.org/10.1016/10.1128/AEM.02289-06.

Luisier, F., Blu, T., Unser, M., 2011. Image Denoising in Mixed Poisson–Gaussian Noise. IEEE Transactions on Image Processing 20, 696–708. doi:https://doi.org/10.1109/TIP.2010.2073477.

Marsh, B.P., Chada, N., Sanganna Gari, R.R., Sigdel, K.P., King, G.M., 2018. The Hessian Blob Algorithm: Precise Particle Detection in Atomic Force Microscopy Imagery. Scientific Reports 8. doi:https://doi.org/10.1038/s41598-018-19379-x.

Meng, Y., Zhang, Z., Yin, H., Ma, T., 2018. Automatic detection of particle size distribution by image analysis based on local adaptive canny edge detection and modified circular Hough transform. Micron 106, 34–41. doi:https://doi.org/10.1016/j.micron.2017.12.002.

Nasr, B., Ahmadi, G., Ferro, A.R., Dhaniyala, S., 2019. Overview of mechanistic particle resuspension models: comparison with compilation of experimental data. Journal of Adhesion Science and Technology 33, 2631–2660. doi:https://doi.org/10.1080/01694243.2019.1650989.

Otsu, N., 1979. A threshold selection method from gray-level histograms. IEEE transactions on systems, man, and cybernetics 9, 62–66.

Qian, J., Peccia, J., Ferro, A.R., 2014. Walking-induced particle resuspension in indoor environments. Atmospheric Environment 89, 464–481. doi:https://doi.org/10.1016/j.atmosenv.2014.02.035.

Raveh-Amit, H., Sharon, A., Katra, I., Stilman, T., Serre, S., Archer, J., Magnuson, M., 2022. Limiting Wind-Induced Resuspension of Radioactively Contaminated Particles to Enhance First Responder, Early Phase Worker and Public Safety—Part 1. Applied Sciences 12, 2463. doi:https://doi.org/10.3390/app12052463.

Rondeau, A., Peillon, S., Vidales, A.M., Benito, J., Uñac, R., Sabroux, J.C., Gensdarmes, F., 2021. Evidence of inter-particles collision effect in airflow resuspension of poly-dispersed non-spherical tungsten particles in monolayer deposits. Journal of Aerosol Science 154, 105735. doi:https://doi.org/10.1016/j.jaerosci.2020.105735.

Sezgin, M., Sankur, B., 2004. Survey over image thresholding techniques and quantitative performance evaluation. Journal of Electronic Imaging 13, 146. doi:https://doi.org/10.1117/1.1631315.

Suji, R., Bhadauria, S.S., 2021. Comparision of Some Image Thresholding Techniques with Morphological Operations and Quantitative Evaluation for Lung Segmentation, in: 2021 2nd International Conference for Emerging Technology (INCET), IEEE. pp. 1–4. doi:https://doi.org/10.1109/INCET51464.2021.9456110.

Theron, F., Debba, D., Le Coq, L., 2020. Local experimental methodology for the study of microparticles resuspension in ventilated duct during fan acceleration. Journal of Aerosol Science 140, 105477. doi:https://doi.org/10.1016/j.jaerosci.2019.105477.

Theron, F., Debba, D., Le Coq, L., 2022. Influence of the transient airflow pattern on the temporal evolution of microparticle resuspension: Application to ventilated duct during fan acceleration. Aerosol Science and Technology 56, 1033–1046. doi:https://doi.org/10.1080/02786826.2022.2120793.

Vincent, J.C., Hill, J., Walker, M.D., Smith, S.A., Smith, S.E., Cant, N.E., 2019. Towards a predictive capability for the resuspension of particles through extension and experimental validation of the Biasi implementation of the "Rock'n'Roll" model. Journal of Aerosol Science 137, 105435. doi:https://doi.org/10.1016/j.jaerosci.2019.105435.

Vrabel, M., Genci, J., Bobik, P., 2017. Low-level computer vision techniques for processing of extensive air shower track images, in: 2017 IEEE 14th International Scientific Conference on Informatics, IEEE. pp. 425–430. doi:https://doi.org/10.1109/INFORMATICS.2017.8327287.

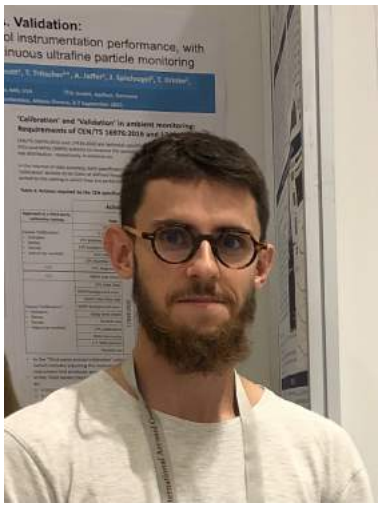

Corentin Cazes is PhD student at IMT Atlantique, GEPEA Laboratory and INRAE, OPAALE Unit. His research focus on microparticle resuspension in transient airflow.

Lionel Fiabane is a Research Engineer in Experimental Fluid Mechanics at INRAE, in the OPAALE Research Unit. His research focuses on fluid dynamics and more precisely on particle transport in air flows, with an interest on the role of turbulence in particle transport, possible particle collective behavior, and more recently microparticles deposition and resuspension from duct walls. His activities are also strongly dedicated to industrial applications in connection with airborne contamination e.g. in ventilated ducts, greenhouses or food processing workshops. He is co-author of 8 publications in peer review journals.

Félicie Theron is Associate Professor in Process Engineering at IMT Atlantique, GEPEA Laboratory. Her research is focused on interactions between air flow in ventilated ducts and microparticles resuspension from duct walls or particle collection by fibrous filters. She is co-author of 14 publications in peer review journals.

Dominique Heitz is a senior research scientist at INRAE, Rennes, France, in the OPAALE research unit, where he has been the ACTA group head since 2013. He received the PhD and habilitation degrees in fluid mechanics. He works on experimental, numerical, and theoretical studies of turbulent flows, with applications in food, agriculture, and environment. Currently his research is mostly focused on developing efficient models and methods for 3D particle tracking, and vector fields reconstruction from image sequences of turbulent flows. Key challenges are the coupling of image sequences with numerical simulation of dynamical laws.

Laurence Le Coq is Professor in Environmental Engineering at IMT Atlantique, GEPEA Laboratory. Her research activitiy deals with mass transfer and particle transport through porous media. She is author of more than 65 publications in international peer-review journals and more than 80 communications in international congress. Her scientific skills are related to : - Aerosol : Transport, capture and resuspension at fluid/solid (porous) interface – application to air depollution and gas separation. - Gaseous pollutants : Transfer w/w.o. reaction at fluid/solid (porous) interface – application gas adsorption. - Porous media : Structural and physico-chemical characterisation – application to carboneceous adsorbant and filter clogging.